Additive Manufacturing 88 (2024) 104256

Contents lists available at ScienceDirect

Additive Manufacturing

journal homepage: www.elsevier.com/locate/addma

Understanding the high-temperature deformation behavior of additively manufactured γ’-forming Ni-based alloys by microstructure heterogeneities-integrated creep modelling

Venkatesh Pandian Narayana Samy [a,*], Frederike Brasche [a], Fuyao Yan [b], Ivo Šulák [c], Betül Bezci [a], Benedikt Nowak [d], Ida Berglund [b], Ulrich Krupp [a], Christian Haase [a,e]

[a] RWTH Aachen University, Steel Institute, Chair Materials Engineering of Metals, R308, Intzestraße 1, Aachen 52072, Germany
[b] QuesTek Europe AB, Råsundavägen 18A, Solna 169 67, Sweden
[c] Institute of Physics of Materials (IPM), Czech Academy of Sciences, Žižkova 22, Brno 616 00, Czech Republic
[d] VDM Metals International GmbH, Kleffstraße 23, Research and Development Department, Altena 58762, Germany
[e] Technical University Berlin, Chair Materials for Additive Manufacturing, Ernst-Reuter-Platz 1, Berlin 10587, Germany

ARTICLE INFO

Keywords:
Additive manufacturing
Ni-based alloys
Modelling
Simulation
ICME
Creep
Heterogeneities

ABSTRACT

Additively manufactured (AM) alloys present unique and heterogeneous microstructures due to the complex, highly dynamic laser-material interactions. These AM-inherent heterogeneities impede the widespread adoption of AM components, necessitating a profound comprehension of their impact on mechanical properties. Despite extensive research on AM of Ni-based alloys, limited attention has been paid to their creep behavior due to the time-intensive nature of creep tests and the long research cycles. Moreover, experiments and conventional alloy-centric approaches to creep modelling are deemed insufficient in quantifying the effects of AM-specific heterogeneities on creep cavity acceleration and in incorporating the microstructural evolution during creep. To address this critical knowledge gap, a novel computational framework was developed within the structure-property paradigm to unravel the intricate mechanisms governing creep properties. A mechanistic creep model was formulated based on fundamental dislocation creep mechanisms, encompassing dislocation climb-glide motion controlled by γ’ precipitates, grain-boundary-sliding (GBS) resistance resulting from M23C6 carbides, and the kinetics of cavity formation. The framework integrates the in situ nucleation, precipitation, and coarsening of γ’ precipitates during creep by a precipitation model. The results revealed an excellent agreement in terms of γ’ precipitate evolution, creep strain, and strain-rate evolution, the predicted creep life, and times to 1 % strain. By elucidating the intricate interplay between microstructural heterogeneities and creep behavior on the cavity nucleation and GBS mechanisms, the developed computational framework provided valuable insights for enhancing the performance of Ni-based alloys manufactured through AM.

1. Introduction

Materials used in high-temperature applications, particularly in industries such as aerospace and energy generation, require a challenging combination of properties, including exceptional strength, toughness, and resistance to creep deformation [1–6]. In that respect, Ni-based alloys have emerged as a prominent and widely utilized class of materials due to their remarkable strength and durability under elevated temperature conditions [7–9]. Alloy 699XA (UNS N06699 EN Alloy number 2.4842) is a NiCrAl alloy designed for i.a. applications in the petrochemical industry and characterized by excellent metal dusting resistance [10,11]. Additive manufacturing (AM) offers an alternative production technique in comparison to conventional manufacturing (CM) with additional advantages like design freedom and near-net-shape production [12]. AM also enables the integration of multiple parts within an assembly into a singular component. This integration yields numerous benefits, including the reduction of overall weight, manufacturing time, processing steps, cost, and complexity [13]. In addition, CM of Ni-based alloys faces challenges due to work hardening and γ’ precipitation during processing leading to expensive post-processing requirements. While AM offers an alternative by suppressing γ’ formation due to the elevated temperature gradients and

---

* Corresponding author.
E-mail address: vnrayana@iehk.rwth-aachen.de (V.P. Narayana Samy).

https://doi.org/10.1016/j.addma.2024.104256
Received 19 February 2024; Received in revised form 6 June 2024; Accepted 12 June 2024
Available online 19 June 2024

high cooling rates during the laser powder bed fusion (LPBF) processes, making it viable for processing Ni-based alloys [14,15].

Despite the numerous advantages offered via AM [13,16], the process introduces its own challenges. The highly localized heat input from the focused laser beam and the subsequent rapid solidification during AM introduces extreme temperature gradients within the part, which consequently leads to a high level of residual stress and internal process-induced defects (e.g. cracks and pores) [17–20]. Furthermore, the complex thermal conditions during AM lead to heterogeneities such as irregular grain structures with pronounced crystallographic texture, chemical microsegregation, and formation of metastable phases within the as-printed products, resulting in unreliable mechanical properties [21–24]. These heterogeneities do not only affect the room-temperature properties but also strongly the creep behavior. Kuo et al. [25,26] reported a poor creep life of AM IN718 compared to CM IN718. This discrepancy was attributed to the concentrated in-homogeneous δ-phase precipitation localized in the interdendritic regions due to Nb segregation, which contrasts with the uniform distribution seen in CM IN718. Additionally, AM IN718 exhibited high initial dislocation density and sub-grain boundary formation, further contributing to its inferior creep performance. Thus, understanding the impact of these AM-specific heterogeneities on creep properties is essential for structural high-temperature applications. The long research cycles and time-consuming nature of creep experiments have hindered comprehensive investigation of AM Ni-based alloys, resulting in a disproportionately lower number of studies. Moreover, the limited number of publications available on creep behavior in AM Ni-based alloys compared to their CM counterparts exhibits inconsistency in reporting creep properties. Some studies have indicated inferior creep behavior [25,27–29], whereas others have reported superior creep characteristics [21,30,31]. This underscores the pressing need for further exploration and comprehension of creep performance in AM materials. The well-established damage mechanisms and structure-property relationships developed for CM alloys cannot be readily applied to AM alloys due to the unique AM-specific heterogeneities [29]. The key parameters such as activation energy, threshold stress, and the power law exponent analyzed from creep experiments performed on the NiCrAl alloy provided valuable insights into the rationalization of creep behavior [32]. However, achieving a comprehensive understanding of the interplay of the mechanisms and the parameters governing creep rates at different stages were absent, requiring the utilization of complex in situ creep characterization techniques [33]. To address these challenges, advanced computational and modelling techniques become indispensable in unraveling the intricate structure-property relationships that are specific to AM alloys [34,35].

Unlike hardness, strength and toughness, creep and fatigue represent dynamic structure-sensitive properties, where the formulation of predictive models is more complex [36]. In the realm of modelling creep behavior, empirical approaches have been the dominant methodology [37–39]. The crux of the limitations associated with empirical approaches stems from the assumption that the creep mechanism (and consequently, the activation energy) remains constant, irrespective of changes in stress or temperature. However, this assumption is often inaccurate, as many creep deformation mechanisms were proposed for different temperature regimes and stresses, such as isolated and continuous stacking faults [40,41], anti-phase boundary shearing [40,42], dislocation climb [43,44], microtwinning [45] and grain-boundary sliding (GBS) [46]. It is worth noting that these mechanisms can operate simultaneously and with varying contribution under different conditions [29]. Addressing these limitations highlights the necessity for a more comprehensive and physics-based model that can encompass the intricate interplay of different creep mechanisms in advanced materials. A physical model effectively accounts for changes in creep strength as a function of the microstructure evolution at different temperatures and stresses, potentially accelerating the discovery of novel materials with improved creep resistance [6,7,12,13].

Although dislocation and GBS modelling approaches are commonly used for creep simulation in CM and AM alloys, a complete understanding of the creep behavior is not possible without understanding the creep cavitation damage [47]. The dislocation creep mechanism typically plays a minor role in the tertiary creep stage. Cavitation is crucial for AM alloys, as the nucleation and growth kinetics are significantly accelerated due to AM-specific heterogeneities, such as intermetallic phases, smaller grains, defects, and microsegregation [29,48,49]. Wu et al. [29] modeled the creep behavior based on continuum damage mechanics (CDM) including the cavitation mechanism. The modelling approach facilitated an in-depth understanding of the impact of AM-specific microstructure parameters on cavitation behavior. It is essential to note that the model did not account for the dynamic evolution of precipitation during creep, while this is indispensable for NiCrAl as γ' evolved during creep. Furthermore, the model validation was carried out under rigorous conditions of high stresses, extending only up to 300 h, revealing cavitation exclusively as the rate-controlling mechanism. Consequently, the intricate interplay and interdependencies between diverse failure mechanisms remained to be explored in more detail.

While there is a limited number of studies addressing the impact of AM-induced heterogeneities on mechanical properties, there is a noticeable absence of numerical approaches to quantifying these effects. Consequently, the utilization of these materials necessitates a comprehensive evaluation of both the kinetics governing the evolution of AM microstructures and the consequential impact of these changes on mechanical properties. Additionally, the phenomenon of in situ γ' precipitation during creep at 750 °C, in the absence of an aging treatment, represents an intriguing area warranting thorough investigation. Thus, the objective of the study is (i) to establish an integrated computational materials engineering (ICME) framework to analyze the effects of AM-induced heterogeneities on the creep behavior and to compare them to CM (referred to as "AM state" and "CM state" respectively throughout the paper), and (ii) to investigate the effect of AM-specific heterogeneities on creep behavior. Therefore, the development of the process–structure and structure–property models will enhance the understanding and application of AM alloys [36].

2. Methods

2.1. Thermodynamic modelling

Phase stability at the equilibrium condition was modeled based on the CALPHAD (CALculation of PHAse Diagram) approach [50] using the Thermo-Calc® software version 2023b [51], and the TCNI12 thermodynamic database [52]. The results were then compared to phase characterization results for AM and CM states. To determine the solidification path and the redistribution of elements, the Scheil-Gulliver model [53,54], integrated into the Thermo-Calc® software, was employed. The model establishes a local equilibrium at the interface between the solid and liquid phases, assuming an ideal mixing of elements in the liquid phase and no diffusion in the solid phase. The approximation effectively captures the microsegregation phenomena that occurs during rapid solidification processes.

2.2. Precipitation Simulation

The kinetics of γ' precipitation from the disordered, face-centered cubic (fcc, γ) matrix during aging heat treatment at 750°C were simulated using the Thermo-Calc® software package with its precipitation module (TC-PRISMA) [51], which is based on the Langer-Schwartz theory and adopts the Kampmann-Wagner numerical method to simulate the concurrent nucleation, growth and coarsening of precipitates in multicomponent and multiphase alloys [51]. TCNI12 [52] and MOBNI6 [55] were utilized as multicomponent thermodynamic and mobility databases, respectively. The NiCrAl alloy composition for γ'/γ simulation was first obtained by excluding high-temperature carbides from the overall composition, based on the equilibrium calculation at the solution temperature. Heterogeneous nucleation of γ' was assumed, with the number of nucleation sites calculated based on the dislocation density of the thin foil characterized by transmission electron microscopy (TEM) [32]. The Thermo-Calc® simplified growth-rate model was used assuming a spherical morphology of nuclei/precipitates. A size-dependent interfacial energy function was applied to represent the γ'/γ coherency transition.

2.3. Creep life modelling

In different stress and temperature regimes as well as in different microstructural conditions, creep mechanisms differ and split across the three stages, primary, secondary, and tertiary. Typically, Ni-based alloys exhibit deformation in the matrix due to a dislocation-based mechanism (ε_{matrix}) or at the grain-boundary due to sliding (ε_{gb}). These mechanisms occur sequentially, with dislocations being relieved from the matrix and supplied to the grain-boundary for GBS, and the resulting deformation strain rates being additive [46,56]. The high-temperature creep deformation of NiCrAl alloy was attributed to contributions from both GBS and dislocation creep (**c.f** Fig. 1**)**. The total creep strain rate in the material can be described as,

$$\frac{d\varepsilon}{dt} = \frac{d\varepsilon_{matrix}}{dt}\left(\gamma', grain\ size\right) + \frac{d\varepsilon_{gb}}{dt}\left(carbides, grain\ size\right) \quad (1)$$

During the dislocation-climb process, the creep deformation is mainly governed by the glide of dislocations. Thus, according to the Dyson's approach [57], the dislocation creep in precipitation-strengthened alloys is based on the jerky glide mechanism, as shown in the Fig. 1**a**. The jerky glide refers to the climb-glide motion of dislocations around the precipitate at stresses below the yield stress. The model is valid only for the climb-glide mechanism at low stress below Orowan bowing or precipitate shearing. An explicit relationship between the matrix shear creep rate and microstructure is given as

$$\frac{d\varepsilon_{matrix}}{dt} = 1.6DC_jM^{-1}\rho_m V_f\left(1 - V_f\right)\left[\left(\frac{\pi}{4V_f}\right)^{\frac{1}{2}} - 1\right]\sinh\left(\frac{\sigma b^2\lambda_m}{MkT}\right) \quad (2)$$

, where ε_{matrix} is the matrix creep strain, ρ_m is the matrix dislocation density, V_f is the volume fraction of the precipitates, λ_m is the average inter-precipitate spacing, C_j is the jog density coefficient, D is the self-diffusion coefficient, σ is the applied stress, b is the Burgers vector, M is the Taylor factor, k is the Boltzmann constant, and T is the temperature.

Dislocation sources become active once the local matrix shear stress (τ_m) surpasses the shear network strength (τ_{net}). Moreover, the presence of coherent particles induces micromechanisms such as particle shearing and Orowan looping, resulting in a strain rate-insensitive athermal shear yield strength (τ_{ath}). Therefore, the creep model applies only when the matrix shear stress falls within the range ($\tau_{net} < \tau_m < \tau_{ath}$). Consequently, at stresses beyond this range, the climb/glide particle bypass micromechanism no longer governs the rate control.

The creep rate equation was coupled with CDM to estimate the pace of transformation of each pertinent microstructural aspect and to project the corresponding degradation in creep resistance. The primary creep stage was predicted by incorporating back stress originating from the plastically deforming matrix acting on the hard, elastically deforming precipitates. This back stress was subtracted from the applied stress σ, and it approached a saturated limit σ_k^*, which was assumed to be due to dislocation punching at the interface between the precipitates and matrix. The evolution of dislocation density is given by an unbounded mobile dislocation multiplication term, D'_d.

$$\frac{d\varepsilon_{matrix}}{dt} = \dot{\epsilon_0}\left(1 + D'_d\right)\sinh\left(\frac{\sigma(1 - H)}{\sigma_0}\right) \quad (3)$$

, where, $\dot{\epsilon_0} = 1.6DC_jM^{-1}\rho_m V_f\left(1 - V_f\right)\left[\left(\pi/4V_f\right)^{\frac{1}{2}} - 1\right]$, $H = \sigma_k/\sigma$ is the hardening parameter, $H^* = 2V_f/\left(1 + 2V_f\right)$ the saturated hardening limit and $\sigma_0 = \left(MkT/b^2\lambda_m\right)$ the stress constant. The evolution of dislocation density is defined as $D'_d = \left(\frac{\rho_{m,i}}{\rho_m}\right) - 1 = C\dot{\epsilon_c}$, where $\rho_{m,i}$ is the initial dislocation density, $\rho_m$is the dislocation density and C is the material constant termed as dislocation multiplication coefficient. The evolution of the hardening parameter towards the saturation limit is given by the platen model [44] as

$$\dot{H} = \frac{V_f E}{\sigma}\left(1 - \frac{H}{H^*}\right)\dot{\epsilon}_{matrix} \quad (4)$$

Furthermore, the grain-boundary carbides provide a back stress against dislocation climb and glide [46,58]. As dislocations pile up at the grain-boundary particles, a back stress is generated against dislocation

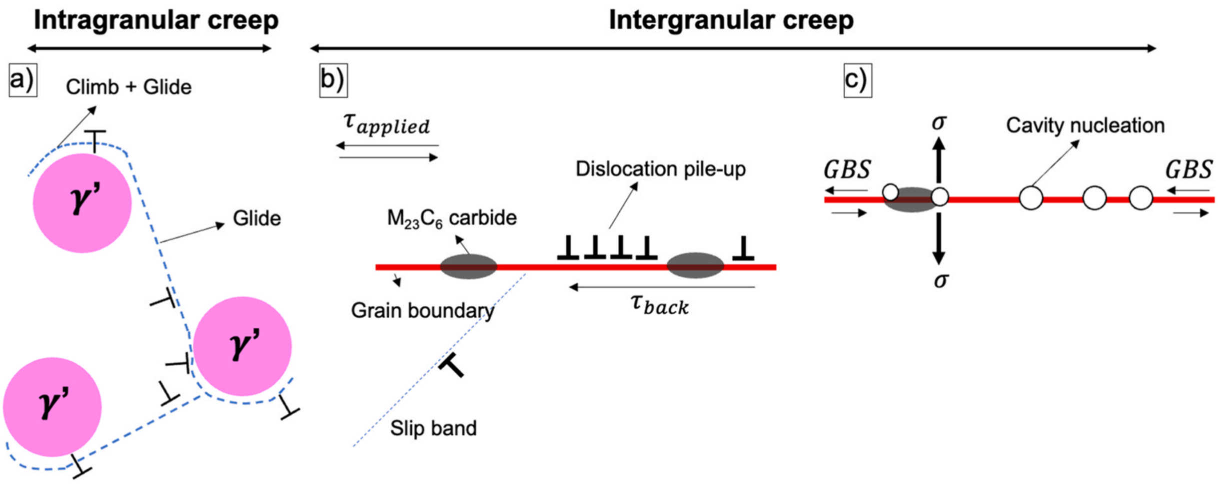

Fig. 1. Creep mechanisms considered in the modelling approach influencing the intragranular and intergranular creep deformation. (a) Combined climb and glide behavior of dislocations within the γ matrix and interaction with γ' precipitates was considered as the rate-controlling mechanism for intragranular creep deformation according to Dyson's model [57]. (b) Dislocation pile-up at grain boundaries due to hindrance from the grain-boundary carbides ($M_{23}C_6$) [58]. (c) Cavity nucleation mechanism at the grain-boundary due to GBS and nucleation at the interface of grain boundary and $M_{23}C_6$ carbides [59].

glide and climb, as shown in Fig. 1**b**. Thus, the rate equation for the transient strain rate due to grain-boundary particles can be expressed as

$$\frac{d\epsilon_{gb}}{dt} = A\frac{D_{gb}\mu b}{KT}\quad\left(\frac{b}{d_{grain}}\right)^{q}\left(\frac{r_{gb}+\quad\lambda_{gb}}{b}\right)^{q-1}\frac{\left(\frac{\sigma}{M}-\quad\tau_g\right)\left(\frac{\sigma}{M}-\quad\tau_c\right)}{\mu^2} \tag{5}$$

where A is a material parameter, D_{gb} is the grain-boundary diffusion, μ is the elastic shear modulus, d_{grain} is the mean grain size, q is carbide distribution parameter, r_{gb} is the mean carbide radius, $\lambda_{gb}$is the mean carbide spacing, τ_g is the glide resistance and τ_c is the climb resistance.

At elevated temperatures, creep initiates the formation and growth of nanoscale cavities heterogeneously at geometrical or microstructural irregularities, as shown in Fig. 1**c**. This continuous process occurs through the diffusional transfer of atoms from grain boundaries to cavities. The growth and nucleation of the cavities follow classical nucleation theory (CNT), which is based on the initial works of Zeldovich [60], Frenkel [61], Becker and Döring [62], Volmer and Weber [63]. Furthermore, Meixner et al. [64,65] implemented the Kampmann-Wagner framework for cavitation kinetics modelling to simulate the nucleation and growth of multiple cavities of various time-steps and sizes. The cavitation kinetics in the grain boundary and around the precipitate are considered through the following equations

$$\dot{I} = N_{GB}\frac{A^*}{\sqrt[3]{\Omega^4}}\exp\left(\frac{-Q_v}{kT}\right)D_{GB}\sqrt{\frac{\Delta F^*}{3\pi RT}}\frac{1}{n^*}\exp\left(-\frac{\Delta F^*}{RT}\right) \tag{6}$$

where N_{GB} is the number of available cavity nucleation sites in the grain-boundary, A^* is the surface area of a critical cavity, Ω is the atomic volume, Q_v is the vacancy formation energy, $\Delta F^*$is the Helmholtz free energy for cavity nucleation, and R is the gas constant. Detailed derivation and explanation of the factors is stated in [29,59,64–66]. The growth of the cavities is further described by

$$r_{\dot{cavity}}\quad = \frac{D\Omega\dot{X}_v}{kTr}\quad\left(\sigma - \frac{2\gamma}{r}\right) \tag{7}$$

where γ is the surface energy between the precipitate and matrix. Failure during the tertiary creep is due to the intergranular failure caused by inter-linking of the cavitation at the grain boundaries. In order to model the coalescence and the crack growth, a deeper physical understanding would be required to comprehend the interaction between two cavities, cavity nucleation locations and the spacing between the cavities. Thus, according to [59] the failure criterion in this study is taken as

$$2r_{cavity\ mean} \geq d_{cavities} \tag{8}$$

where $r_{cavity\ mean}$ is the mean cavity radius and $d_{cavities}$ is the mean inter-cavity spacing. The creep cavitation mechanism was considered as a strain-induced damage by an effective stress through physics-based continuum creep damage mechanics [67].

$$\dot{\sigma_e} = \quad\frac{\sigma}{(1-D_N)} \tag{9}$$

$$\dot{D_N} = \quad \dot{\epsilon_a} I\pi \quad {r_{cavity}}^2 \tag{10}$$

where D_N is the cavitation damage parameter. To summarize, the simulation model utilized in this study includes the contributions of creep deformation caused by γ' precipitation, dislocation climb, GBS, and cavity growth kinetics.

2.4. Model setup

Due to the complexity of the initial microstructure, the microstructure characteristics were extracted and simplified as input to the model. A schematic of the microstructure evolution during creep is shown in

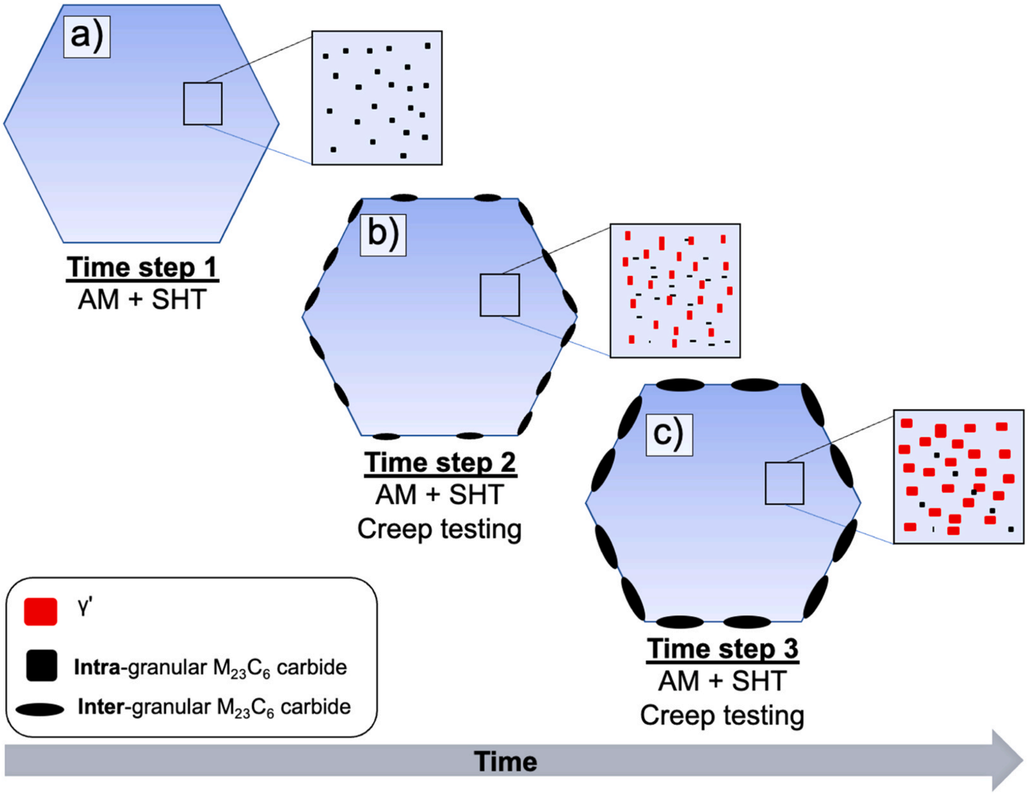

Fig. 2. Hierarchical microstructural features modelled in the study illustrating (a) the initial state with primary nanosized intragranular $M_{23}C_6$ carbides, (b) precipitation of γ' in the matrix and $M_{23}C_6$ carbides at the grain-boundary and the dissolution of primary nanosized intragranular carbides and (c) coarsening of the intergranular carbides and γ' precipitates.

Fig. 2. In its initial state (solutionized, SHT), the NiCrAl alloy featured a fcc (γ) matrix with primary nanosized intragranular $M_{23}C_6$ carbides. During creep at 750 °C, a significant microstructural transformation occurred: the nucleation and precipitation of the γ' phase within the matrix and the precipitation of $M_{23}C_6$ carbides at grain boundaries. These phenomena had a substantial impact on the material behavior during creep, as γ' precipitates hinder dislocation glide, while $M_{23}C_6$ carbides constrain GBS. It is noteworthy that the primary nanosized intragranular $M_{23}C_6$ carbides, characterized by smaller volume fractions in AM state and larger sizes in CM state, played a negligible role in the dislocation glide mechanism and were therefore excluded from the modelling approach.

The microstructural parameters employed in the creep model were derived from various experiments, including scanning transmission electron microscopy (STEM), electron back scattered diffraction (EBSD), inverse pole figure (IPF) maps, scanning electron microscopy (SEM), and energy dispersive X-ray (EDX) analyses, as summarized in Table 2. The MATLAB code utilized the results of precipitation simulations and cavity nucleation to iterate the γ' volume fraction, radius, and the cavity density in the creep simulations. The physical parameters of the model were obtained from various previous studies, as shown in Table 1. Notably, the determination of C_j proved challenging and thus, required calibration within the model [29,44,68]. C_j indicates the effectiveness of jog formation when encountering a precipitate. Additionally, the material constant (A) was calibrated based on experimental results. These parameters remained consistent for both AM and CM states across all temperatures and stresses investigated in this study. Cavity growth of pre-existing cavities occurred at each time-step, with concurrent generation of new cavities. The grain-boundary area allocated for cavities was diminished by the space occupied by preexisting cavities in each time step. These iterative procedures persisted until the predefined failure criterion was satisfied. Coalescence and crack growth processes have not been explicitly modeled in the current study. These processes typically involve complex interactions between multiple cavities, which require a more in-depth understanding for accurate modelling. Additionally, coalescence represents the final stages of creep failure [64]. Porosity can be incorporated into the current model as pre-existing cavities, defined by the cavity nucleation rate. This would result in an initial cavity number density of 5.1×10^{11} m^{-3} for a porosity of 0.43 % as seen in the experiments [32]. However, when compared to the potential cavitation sites at grain boundaries (activated sites: 10^{14} m^{-3}; total sites: 10^{24} m^{-3}), this amount is minimal. Gas pores are uniformly distributed throughout the sample, predominantly situated in the interior of the melt pool. Consequently, they exhibit no discernible impact on the processes of cavity nucleation and growth, as their growth rate is confined [49]. Furthermore, Ulbricht et al. [69] demonstrated, via interrupted CT scan studies, that the initial porosity did not influence the progression of creep damage in the highly dense 316 L specimens fabricated by LPBF. Thus, due to the high density of the AM state with no defects except for gas pores and heavily cavitated grain boundaries (c.f Fig. 4a), pores didn’t influence the creep mechanism and hence omitted from the creep modeling framework.

Table 1
The material parameters used in the creep modelling approach for AM and CM states.

Physical parameters	Description	Value	Ref.
Q	Activation energy ($kJmol^{-1}$)	305	[44]
C_j	Jog density coefficient	0.002	-
D_o	Pre-exponential diffusivity (m^2s^{-1})	1.9×10^{-4}	[44]
b	Burgers vector (Å)	2.54	[44]
M	Taylor factor	3.1	[44]
k	Boltzmann’s constant ($m^2kgs^{-2}K^{-1}$)	1.38×10^{-23}	-
E	Young’s modulus at room temperature (GPa)	160	[44]
A	Material constant	2×10^4	[29]
$D_b\delta_b$	-	3.5×10^{-15}	[29]
$\gamma_{carbide}$	Interface energy carbide (Jm^{-1})	1	[29]
γ_{gb}	Interface energy grain boundary (Jm^{-1})	0.69	[29]
γ_o	Surface energy of matrix (Jm^{-1})	1.73	
σ_D	Driving force of defects (Pa)	1.2×10^{10}	[64]
Q_v	Vacancy formation energy (eV)	1.7	[64]
Ω	Inter-atomic spacing (m)	1.0710×10^{-29}	[64]
a	Atomic volume (m^{-3})	2.24×10^{-10}	[64]

Table 2
The numerical parameters used in the creep modelling approach of AM state.

Microstructure parameters	Description	CM	AM	Ref.
ρ_m	Dislocation density (m^2)	2.1×10^{13}	5.1×10^{13}	Experiments
T	Creep temperature (°C)	750	750	Experiments
σ	Creep stress (MPa)	100–200	100–200	Experiments
σ_D	Driving force of defects (Pa)	1.2×10^{10}	1.2×10^{10}	[64]
d_{grain}	Grain size without twins (μm)	60	32	Experiments
r_{gb}	Carbide size (μm)	0.95	0.37	Experiments
λ_{gb}	Carbide spacing (μm)	1.257	0.625	Experiments
v_f	Final γ' volume fraction (%)	10.95	11.8	Experiments
r	Final γ' radius (nm)	55	60	Experiments
N_s	Nucleation sites ($x10^{24}$ $/m^3$)	1.32	3.17	Calculated

2.5. Experiments

The nominal composition of Alloy 699XA is given in Table 3**.** The CM state was produced by hot rolling and subjected to a SHT. The AM state samples were fabricated by means of LPBF on an EOS-M290 system using an Yb fiber laser. The printing process was operated at a laser power of 260 W and a scanning speed of 1100 mm/s. The hatch distance, layer thickness and the preheating temperature were 110 μm, 40 μm and 80 °C, respectively. Furthermore, the as-built state was also subjected to SHT. No aging heat treatments were performed as the commercial alloy is intended to be operated around the aging temperature and thereby γ' precipitation occurs during service. With respect to the alloy’s extensive application in petrochemical industries at high temperatures (>500 °C), creep testing was performed at 750 °C close to common service conditions for 699XA. The yield strength of AM and CM states after SHT was 265 MPa and 260 MPa, respectively, and the tensile strength was 483 MPa and 481 MPa, respectively, at 750°C [32]. While the applied creep stresses ranged between 100 – 200 MPa (Table 2). A detailed description of AM processing, creep experiments, characterizations, and further analysis are referred to [32].

3. Results

3.1. Experimental findings

The AM state specimens were manufactured utilizing gas-atomized powders with a composition measured by EDX point analysis 2.3 wt% Al, 29.1 wt% Cr and 0.1 wt% Fe. The EDX point analysis on the AM state after SHT indicated that grain-boundaries were slightly enriched with Al

Table 3
Nominal composition of NiCrAl alloy (Alloy 699XA, VDM Metals GmbH, Germany) [11].

	Ni	Cr	Al	Fe	Mn	Si	Ti	Nb	Cu	Zr	C	N	P	S	B
min	Bal.	26.0	1.9	-	-	-	-	-	-	-	0.005	-	-	-	-
max	Bal.	30.0	3.0	2.5	0.50	0.60	0.60	0.50	0.50	0.10	0.100	0.05	0.02	0.01	0.008

(2.35 wt%) and Cr (31.78 wt%) compared to the matrix with Al (2.09 wt %) and Cr (27.92 wt%). Hence, only a minor loss of elements like Al was observed in the study after AM [32]. Fig. 3**a-f** shows the microstructural characterization of AM and CM states after SHT by EBSD and TEM. Annealing twins were present in both AM and CM states due to the low stacking fault energy (SFE) in Alloy 699XA [70,71], as shown in the EBSD-IPF maps (c.f Fig. 3**a, b).** The AM state exhibited a fine-grained, partially recrystallized microstructure due to primary nanosized intragranular $M_{23}C_6$ carbides hindering the grain-boundary migration during SHT (c.f Fig. 3**f**). The high cooling rates and complex thermal conditions in laser material processing lead to fine intragranular nanosized $M_{23}C_6$ carbides in the AM state, compared to coarse carbides in the CM counterpart (cf. Fig. 3**e,f**).

Figs. 3**i** and 3**j** show the γ' precipitates in the γ matrix upon creep for AM and CM states at 750 °C. The γ' precipitates exhibited a spherical morphology and were uniformly distributed in the matrix. The grain boundary precipitates were characterized by SEM-EDX and diffraction patterns based on the synchrotron X-ray diffraction analysis as $M_{23}C_6$ carbides [32], as shown in Figs. 3**g** and 3**h.** A higher volume fraction and uniform distribution of carbides were observed in the AM state. The CM state had a discrete distribution of carbides and lower volume fraction. The intragranular carbides were coarser and did not dissolve completely even after aging for 761 h at 750 °C. The formation of grain-boundary carbides was facilitated by carbon provided in the supersaturated matrix and by dissolution of primary nanosized intragranular carbides. The fine intragranular carbides in the AM alloy dissolved completely and re-precipitated at the grain boundaries during creep testing. The calculated grain sizes, carbide number density and γ'-fraction evolution were used as inputs for the creep model. Upon creep fracture, the AM and CM states exhibited an intergranular fracture, as shown by the EBSD analysis in Fig. 4. The cracks propagated along the grain boundaries, as highlighted in the insets through the kernel average misorientations (KAM) and band-contrast maps at 750 °C and 100 MPa. The SEM analysis of the AM state after failure at 100 MPa revealed that the cavities were formed along the grain boundaries and near the carbide/grain-boundary interfaces in the AM state, causing cavity coalescence and failure [72,73].

3.2. *Thermodynamic and Scheil Simulations*

Equilibrium phase fractions as a function of temperature were predicted, as depicted in Fig. 5**a**. The solvus temperature of the γ' phase was found to be approximately 780 °C, while that of $M_{23}C_6$ (M primarily as Cr) was around 1050 °C. Additionally, the precipitation of MX phase

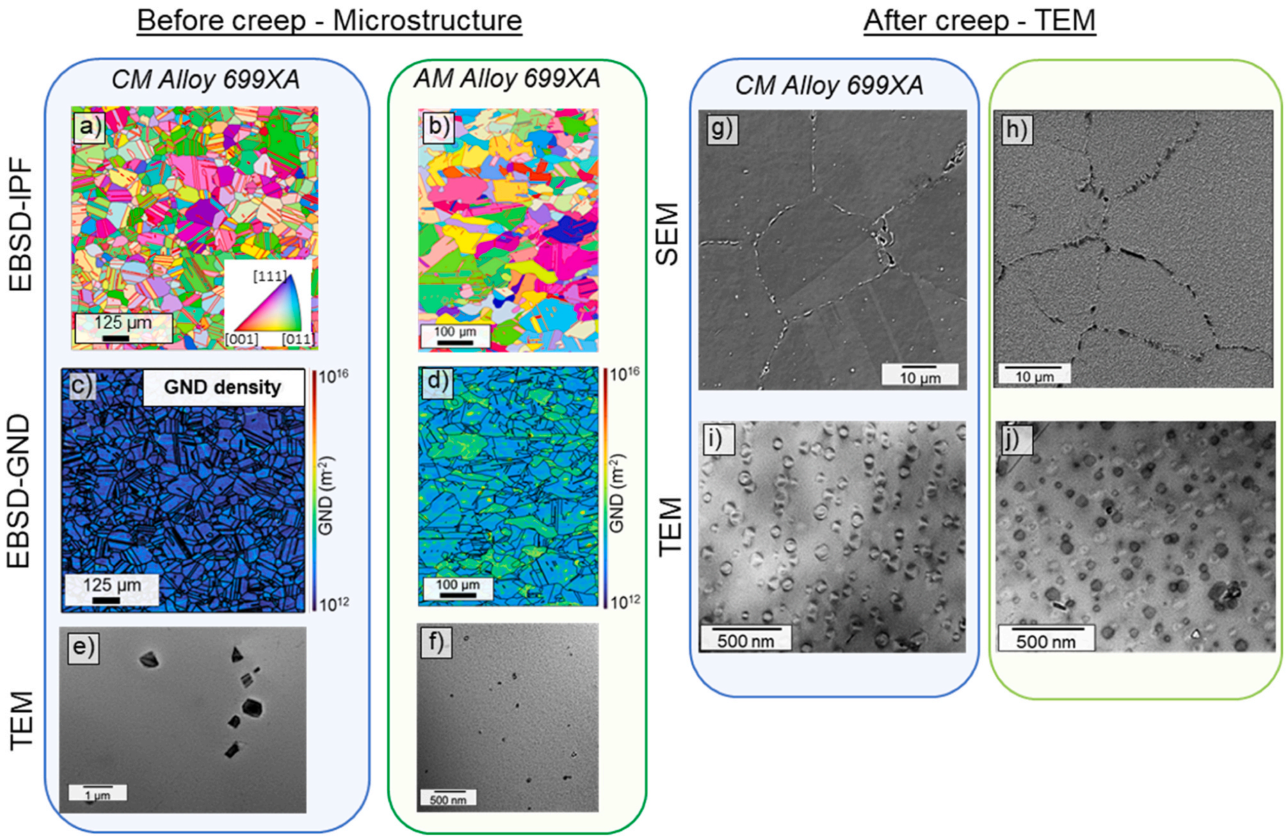

Fig. 3. Multi-scale microstructure characterization of AM and CM states. (a, b) EBSD analysis with IPF color-coding. Twin boundaries and high-angle grain boundaries are highlighted in red and black, respectively. (c, d) Geometrically necessary dislocation (GND) density map calculated from the EBSD data. (e, f) Primary nanosized intragranular $M_{23}C_6$ carbides after SHT. (g-j) Microstructure analysis of AM and CM states after creep at 750 °C and 100 MPa for AM and CM states after 901 h and 761 h, respectively. (i, j) STEM analysis showing the spherical γ' precipitates in the matrix (g, h) SEM analysis showing the grain-boundary carbides ($M_{23}C_6$) in the AM and CM states.

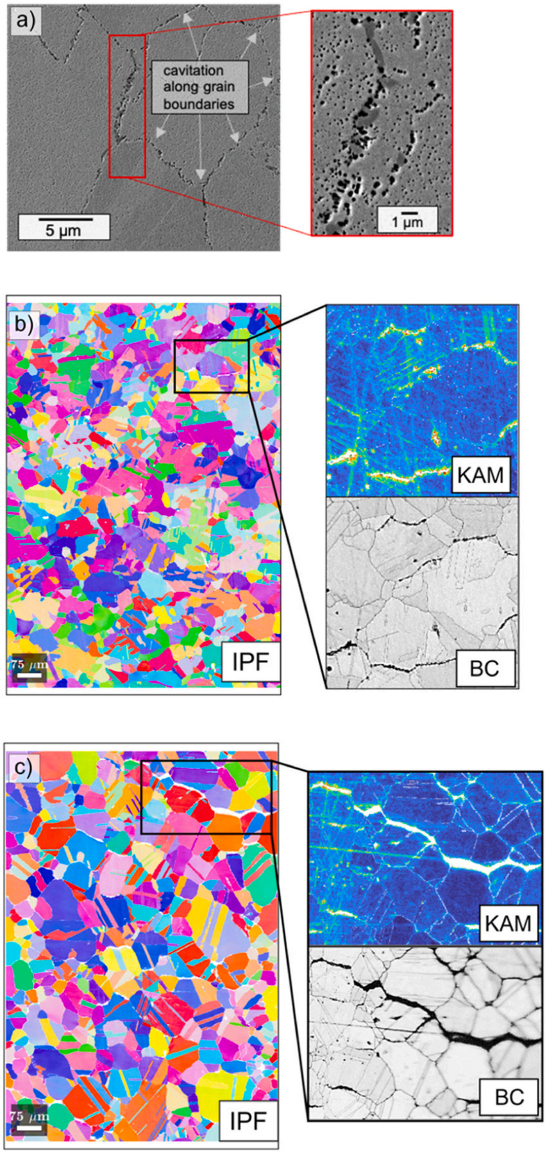

Fig. 4. SEM analysis of CM and AM state after creep fracture at 100 MPa for 761 and 901 h at 750 °C. (a) SE micrograph of the AM state after creep showing the formation of cavities across the grain boundaries and carbide/matrix interfaces during creep. The inset shows the magnified section of the area considered with creep cavities formed along the grain boundary with γ’ in the matrix. (b, c) Intergranular fracture in the AM and CM states after creep, with insets showing the KAM and band-contrast (BC) map after creep fracture.

(primarily in the form of ZrN) was predicted to occur in NiCrAl alloy at temperatures close to or higher than the melting point of the fcc phase. To comprehend the solidification process during additive manufacturing (AM), the solidification pathway of NiCrAl alloy was examined based on the Scheil-Gulliver modelling results, both with and without the addition of nitrogen, as illustrated in Figs. 5**b** and 5**c**. It was predicted that after the initial formation of corundum-type Al_2O_3 phase, fcc-structured γ phase solidified as the primary phase starting from around 1250 °C, and thereafter forms the eutectic structure comprised of MX and $M_{23}C_6$ phases at the end of solidification. These findings align well with the TEM analysis that revealed the presence of ZrN nitrides and intragranular $M_{23}C_6$ carbides in the AM state. In the CM state, no Al_2O3 was observed, as almost no oxygen was contained. Due to the higher cooling rates during LPBF, the volume fraction and particle size of $M_{23}C_6$ carbides in the AM state were lower than those in the CM state. Consequently, this increased the C content dissolved in the γ phase and segregated at grain boundaries, thereby promoting the precipitation of $M_{23}C_6$ carbides, as corroborated in the earlier sections of the manuscript.

3.3. Precipitation Simulation

The simulations of γ’ precipitation in the fcc matrix during aging treatment of NiCrAl alloy were conducted, and the predicted γ’ precipitate size distribution results for the AM state are presented in Fig. 6. Among the various parameters employed, γ’ phase free energy correction, matrix diffusivity, and γ’/γ interfacial energy underwent calibration. The volume fraction of the γ’ phase after 901 h aging at 750 °C was assumed to reach thermodynamic equilibrium, and its value was used to correct the γ’ phase free energy predicted by the TCNI12 database. An error function representing the size-dependent interfacial energy was applied to represent the γ’/γ interface-coherency transition, based on the prior work [74] and with calibration against the characterized precipitate size distribution by SXRD and STEM techniques [32]. In addition, a diffusivity correction factor was applied to the MOBNI6 database to rescale the diffusivity matrix for local fitting. The predicted precipitate radius and volume fraction are presented in Fig. 6, with nucleation site saturation evident as the plateaus in the curves, whereafter particle coarsening takes over. In general, the predicted precipitate size distributions demonstrated good agreement with the experimental data, considering sources of uncertainties arising from experimentation and simulation assumptions. A comparable precipitation behavior was anticipated for the CM state with the same precipitation mechanism [28]. Since the precipitation of γ’ phase is not influenced by the applied stress [75], similar precipitation kinetics were used for the creep modelling approach across different stresses.

3.4. Creep Simulation

Creep simulations were carried out employing the specified parameters detailed in Table 1 and Table 2, as illustrated in Fig. 7. The simulated creep data was then compared with experimental results, revealing a notable agreement between the two datasets for both AM (c.f Fig. 7**a)** and CM (c.f Fig. 7**b**) states at 750°C across a stress range spanning from 100 to 200 MPa. The creep strain evolution clearly indicated the complete absence of the pure secondary creep stage at higher stresses (>100 MPa) due to a transient creep behavior. However, at 100 MPa, the creep behavior distinctly exhibited the three stages, shedding light on the diverse mechanisms operative under varying stress levels. Furthermore, the adoption of a stress-based damage evolution model accurately captured the evolution of creep strain at different stresses (c.f Figs. 7**a** and 7**b**), however, this led to slight over-prediction of the ductility of the material.

Furthermore, the creep strain rate versus time for CM and AM states at 750 °C based on experiments and simulations was plotted, revealing a commendable agreement, as depicted in Figs. 7**c** and 7**d,** respectively. Surprisingly, despite the smaller grain sizes, the minimum creep strain rate in the AM state remained similar to or slightly lower than that of the CM state in the secondary creep regime. This phenomenon was attributed to the uniform distribution of carbides in the AM state, in contrast to the discrete distribution in CM alloy, which constrained the extent of GBS. A noticeable observation from the plots was that at stresses exceeding 100 MPa, the curves exhibited a behavior akin to a steady-state strain rate, while at 100 MPa, a steady-state creep rate behavior was evident.

The comparisons of time to rupture (TTR) and time to 1 % strain between experiments and simulations are illustrated in Fig. 8**a-d**. The inverse relationship of applied stress and creep life suggests a diffusion controlled cavity-growth mechanism [59]. Consequently, it can be concluded that the creep modelling approach effectively captured the mechanisms governing creep deformation at 750 °C for Alloy 699XA over the duration of up to 850 h. These results underscore the accuracy

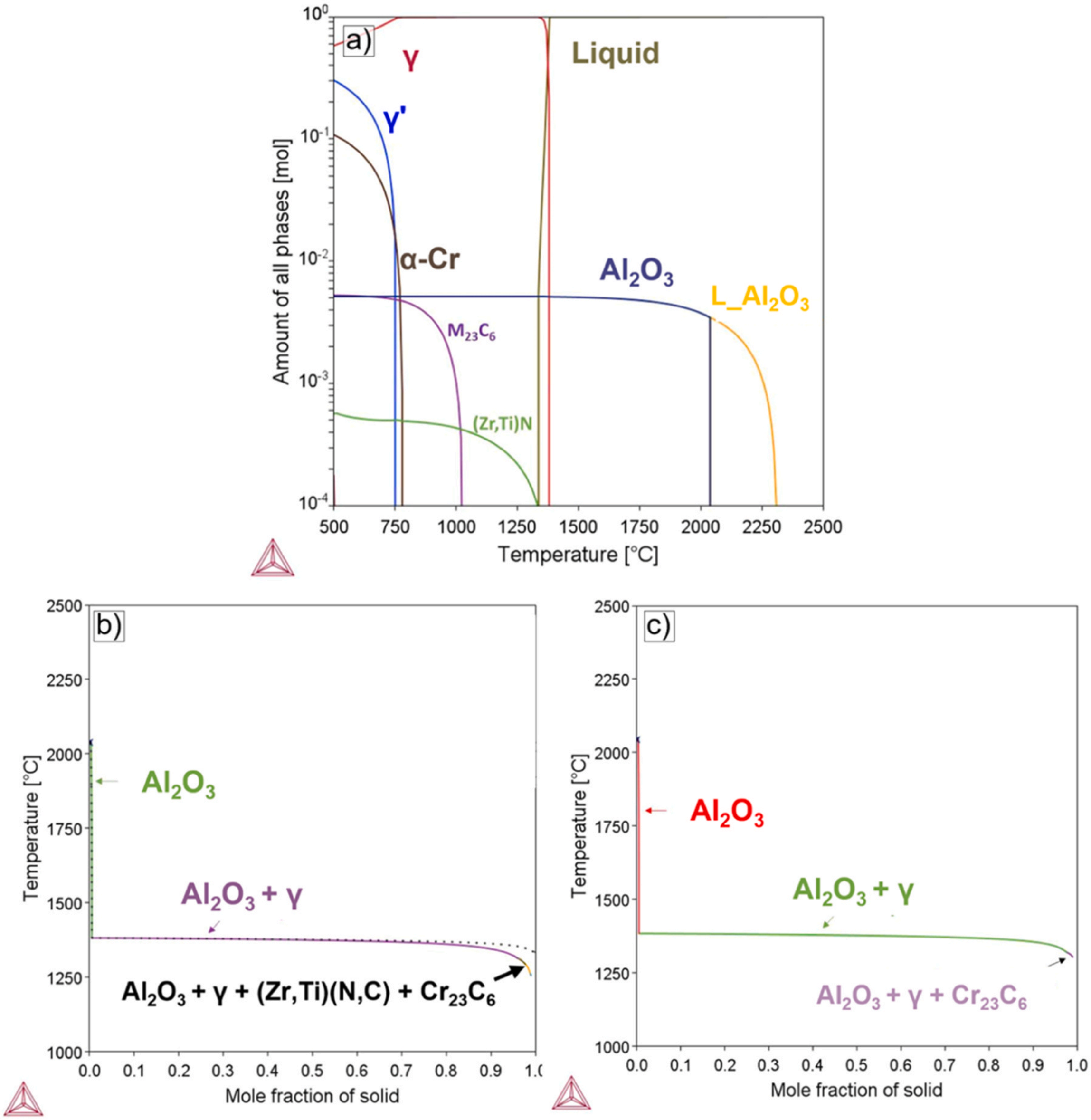

Fig. 5. Thermodynamic simulations for NiCrAl alloy calculated in Thermo-Calc®. Solidification path of NiCrAl alloy calculated by Scheil-Gulliver model (a) with nitrogen (b) without nitrogen. (c) Equilibrium phase fractions of the phases present in NiCrAl alloy.

and reliability of the model for simulating creep behavior in Alloy 699XA, thereby presenting the potential for predicting the mechanical properties of similar alloys under similar conditions.

4. Discussion

Alloy 699XA, a precipitation-strengthened NiCrAl alloy, displayed a similar creep rate in both AM and CM states. The presence of the γ' precipitate within the alloy governed its creep resistance due to dislocation climb, while distinct mechanisms operated at varying stress levels during creep testing at 750 °C. At elevated stresses, such as 200 MPa, even though the volume fraction of γ' precipitates reached 8.2 %, the CM state experienced failure within a mere 21.5 h. Conversely, at 100 MPa, where the volume fraction reached 10.5 %, the samples endured for a significantly higher time to rupture, with failure occurring after 761 h. Furthermore, the AM state exhibited reduced ductility and shorter creep rupture times compared to their CM counterparts, a trend confirmed through simulations, as depicted in Fig. 7. The diminished ductility observed in the AM state was correlated with a decreased lifetime relative to the CM state. The proportionality of time to rupture and ϵ_f (strain at failure) suggested an absence of strain softening or substructure formation. Considering the AM-specific heterogeneities, the NiCrAl alloy featured a smaller grain size and a uniform distribution of carbides after AM. Consequently, it was imperative to comprehend the impact of these heterogeneities on the creep behavior under varying stress conditions.

4.1. Creep cavitation

At elevated stresses, the dominant damage mechanism shifted to accelerated creep through a fracture-damage process [76]. This tertiary creep regime, as evident in Fig. 4**a**, was primarily attributed to grain-boundary cavitation. Experimental observations also confirmed that the NiCrAl alloy failed due to the interlinking of cavities at grain boundaries and around $M_{23}C_6$ carbides at 750 °C. Cavities in materials nucleate at grain boundaries, solute segregation, and at the particle/matrix interfaces [59]. Cavities then grow through a stress-directed and diffusion-controlled process, either through atom diffusion away

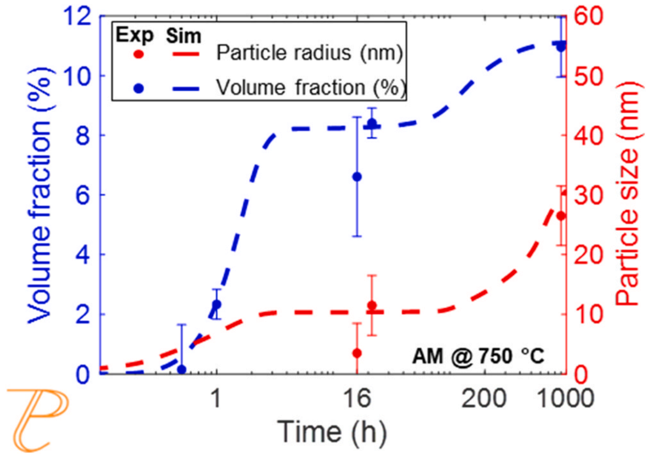

Fig. 6. Calculated precipitation kinetics of γ' phase at 750 °C showing the average volume fraction and precipitate size. The results were compared with the measurements of experimental results from SXRD and STEM in the AM state [32].

from nucleated cavities or vacancy diffusion towards the cavitated regions. It is important to note that cavities below a certain minimum radius (r_c), tend to shrink and disappear rather than grow. Therefore, the rapid nucleation and growth of cavities primarily occurred at grain boundaries (c.f. Fig. 4**c**). The microstructural features contributed to a decrease in surface energy or an increase in local stress concentration, thus lowering the critical size required for cavity nucleation. The cavities were observed and simulated only on grain boundaries and intergranular $M_{23}C_6$/matrix interfaces, since they act as sites of high stress concentration in the microstructure [77]. Cavities were observed exclusively along the high-angle grain boundaries, while the twin boundaries remained unaffected. This phenomenon is attributed to the increased structural order and reduced available volume within coincident site lattice (CSL) boundaries [78]. These conditions hinder the dislocation mobility by impeding vacancy diffusion and climb processes, as well as the absorption and dissociation of extrinsic dislocations essential for GBS and cavity formation. Consequently, no voids were detected at the twin boundaries. Diffusion in grain boundaries is significantly faster than in the bulk, promoting heterogeneous nucleation of cavities. Cavitation was driven by vacancy diffusion in the NiCrAl alloy, initiated in the primary creep regime but at nanometer sizes (5 – 100 nm) and low number densities (10^2 – 10^3 /mm^2). Therefore, cavitation did not control the strain-rate evolution in the primary and secondary regimes, resulting in similar creep behavior for AM and CM states at 750 °C. The coalescence of growing cavities at grain boundaries ultimately promoted decohesion, led to macroscopic crack formation larger than the grain size, which then grew and interconnected, causing intergranular creep fracture.

The cavity nucleation rate directly influences the potential cavity nucleation sites and the time required for cavities to interlink and lead to failure. In the AM state, smaller grain sizes increased the number of available cavity nucleation sites, accelerated the cavity nucleation kinetics, and total nucleated cavities, as shown in Figs. 9**a** and 9**b**. The nucleation rate of the cavities is directly proportional to the applied stress, grain size, diffusion coefficients and vacancy concentrations. Smaller grain sizes further increased the number of diffusion paths for cavity growth, enhancing the growth rate. However, over time, the growth of cavities to larger sizes and accelerated nucleation of more cavities (10^4 /mm^2) shifted the creep rate towards early failure in the AM state compared to the CM alloy. Consequently, creep strain

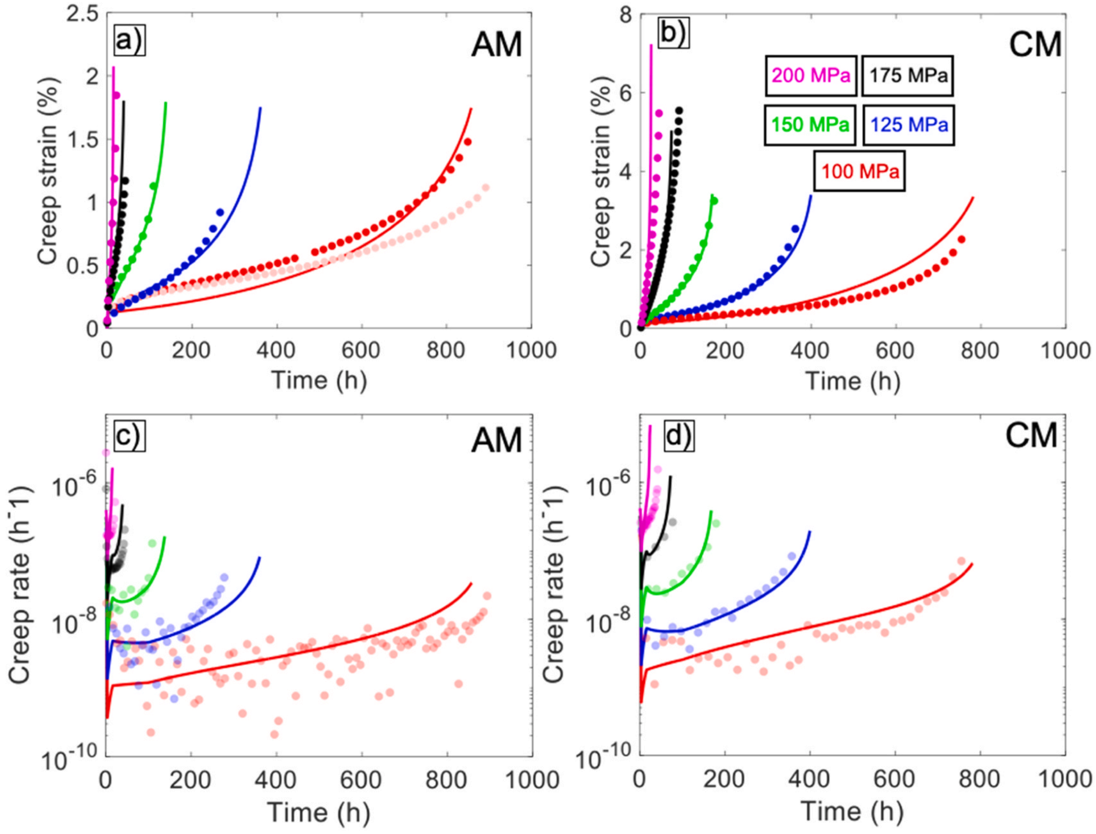

Fig. 7. Comparison of the experimental (points) and simulated data (solid lines) for (a) AM and (b) CM state at 750 °C. The AM state was tested twice at 100 MPa, as shown by the curves with different opacity. Creep-rate evolution over time for the (c) AM and (d) CM state from experiments and simulations at 750 °C and stresses between 100 – 200 MPa.

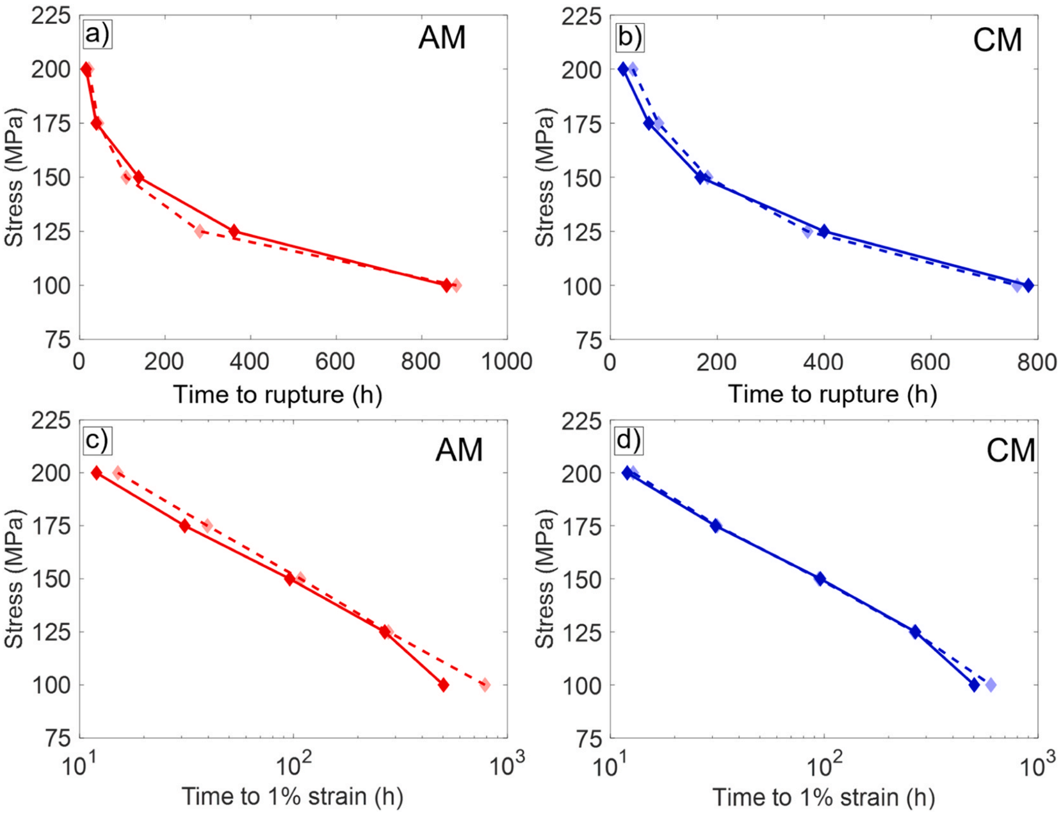

Fig. 8. Simulated (solid lines) TTR diagrams of the (a) AM (red) and (b) CM (blue) state compared with experiments (dashed lines) at 750 °C. Comparison of experimental (dashed lines) and simulated (solid lines) creep life to 1 % strain for the (c) AM and (d) CM state.

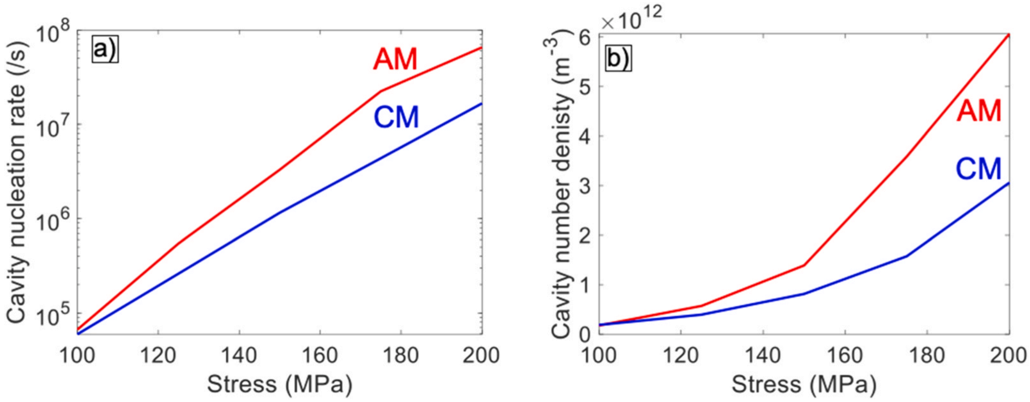

Fig. 9. Simulated cavitation behavior in both AM (red) and CM (blue) state at 750 °C under stress conditions ranging from 100 to 200 MPa. Impact of stress on the (a) mean cavity nucleation rate and (b) final cavity number density.

acceleration primarily occurred in the tertiary creep regime due to increased effective stress (σ_e) and accelerated cavitation damage (D_N) [56,59,77,79]. Additionally, the high dislocation density in the AM state prevented stress relaxation processes at cavity tips, leading to crack propagation upon reaching a critical stress [25]. Higher cavity kinetics resulted in faster cavity inter-linkage and, consequently, a shorter creep life. The cracking behavior and stress relaxation were not included in the current modelling approach, and this explains the slight differences in the creep life between the simulation and experiments.

Moreover, the applied stress, featured in the exponential term of the cavity nucleation rate, exerted the most significant influence. Noticeable differences in cavity nucleation rates and cavity number densities were observed between AM and CM states under varying stress levels, as depicted in Figs. 9**a** and 9**b**. Thus, at higher stresses (>100 MPa), the AM state exhibited a poor creep life compared to the CM state due to a higher grain-boundary density and a higher number density of grain-boundary $M_{23}C_6$ carbides leading to accelerated cavitation.

Fig. 10**a** shows the evolution of the damage parameter (D_N) calculated based on the simulation results. It was clearly seen that until 100 MPa, the D_N was higher for the AM state compared to CM due to the accelerated creep cavitation. However, the effect of cavitation was subdued, and a different mechanism was active at 100 MPa. Fig. 10**b** shows the strain rate evolution based on experiments for CM and two trials of AM state at 100 MPa at 750 °C. It clearly depicts that AM and CM states exhibited a similar steady-state strain rate, however, tertiary creep was accelerated in the CM state. Öberg et al. [80] observed similar behavior in cast steel HK30 at 750 °C and accounted recrystallization for the different creep behavior at low and high stresses. However, no

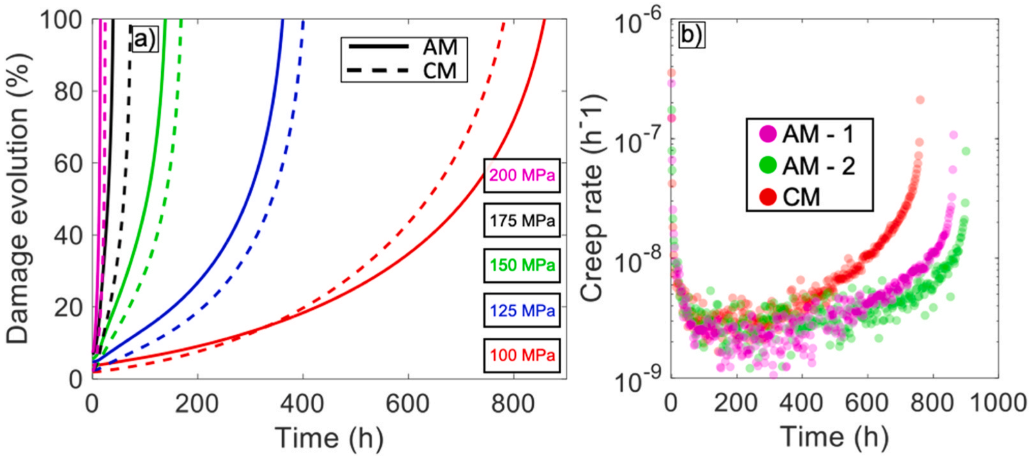

Fig. 10. Simulated evolution of the cavitation damage parameter (D_N) for (a) AM (solid lines) and CM (dashed lines) states at different stresses and (b) experimentally measured evolution of strain rate for both AM and CM states at 100 MPa and 750 °C, including the two trials of the AM states.

(dynamic) recrystallization was observed in the NiCrAl alloy during creep experiments (c.f Fig. 4**b-c**)

4.2. *Grain boundary sliding (GBS)*

The failure of the NiCrAl alloy at high stresses was mainly ascribed to the nucleation, growth, and coalescence of cavities at grain boundaries, ultimately leading to failure. Additionally, GBS is also considered as an important mechanism for creep cavity growth. In the power-law creep region, GBS plays a prominent role towards the creep behavior, especially at low stresses, while dislocation climb dominates at high stresses [81–84]. GBS results in stress concentration at grain-boundary precipitates, grain boundaries and triple points, consequently accelerating the cavity nucleation [59]. Previous studies have noted that GBS does not alter Norton's power law exponent *n*; instead, it significantly contributes only to the creep strain evolution [85]. The significant role of GBS was evident in the NiCrAl alloy, as intergranular cracking was observed in both AM and CM states, as depicted in Fig. 4.

Initially, at high stresses, the intragranular dislocation mechanism and cavity formation dominated the material's creep behavior, as the grain-boundary carbides did not experience prolonged exposure times. Moreover, since cavity nucleation rate and growth were linearly proportional to the applied stresses, significant differences were observed at higher stresses (c.f Fig. 9). However, at 100 MPa, similar creep-cavity nucleation rates and cavity number densities were observed (c.f Fig. 9). At lower stresses, the coarsening of carbides occurred over longer exposure times, diminishing grain-boundary pinning forces and facilitating strong GBS. GBS can typically be accommodated through either grain-boundary migration or recrystallization. However, in this study, the absence of newly recrystallized grains and the similar shape factor observed before and after creep [32], suggested that GBS was not accommodated by either grain-boundary migration or recrystallization. Instead, the predominant mechanism was identified to be dislocation activities, which effectively facilitates GBS [86]. GBS induced substantial stress concentrations within the grain interior, subsequently redistributed at the grain boundaries, thereby diminishing normal stresses in those regions. However, at high stresses, where GBS was minimal, normal stresses at the grain boundaries were not redistributed or reduced, resulting in no significant GBS [85]. Consequently, diffusion-controlled cavity growth became the rate-controlling step at higher stresses.

The accelerated GBS in the CM state at low stresses (c.f Fig. 10**b**) was attributed to the discrete distribution of carbides (c.f Fig. 3**g-h**), which intensified GBS and promoted the formation of creep voids. Since the effective stress and damage accumulation in the model were calculated as a function of the macroscopic strain rate, the contribution of GBS to tertiary creep and creep cavitation was inherently included in the modelling approach ($D_N \, \alpha \, \dot{\varepsilon}$). As the strain rate increased due to GBS, the damage factor increased, leading to earlier failure of CM state (c.f Fig. 10). These findings aligned with experimental results reported by Mancuso et al. [85]. Fig. 11 illustrates the impact of GBS at different stresses and carbide number densities. The variation in carbide number density was a numerical study and does not reflect the material behavior in terms of carbide evolution. At higher stresses, carbide number density had a minimal influence on creep behavior as cavitation dominated. However, at 100 MPa, as the carbide number density increased from 0.5 to 2.5 $\times 10^{-10}$ / m^2, creep life extended from 320 to 740 h. The effect of carbide number density on creep life diminished as stresses increased to 125 MPa and 150 MPa. At lower stresses, GBS had a more significant impact, leading to the early acceleration of strain rate in CM state, particularly due to its lower resistance to GBS. As the cavity damage parameter was directly proportional to the strain rate, it contributed to the early onset of tertiary creep in CM state, especially at lower stresses. Hence, there is no optimal grain size that can provide maximized creep properties over a wide temperature and stress range [87]. Thus, on the one hand, the augmentation of intergranular carbide density diminished the occurrence of GBS, thereby yielding an enhanced creep lifetime, particularly under lower stresses. On the other hand, an increase in grain size mitigated the acceleration of tertiary creep rates, consequently enhanced the creep lifetime, especially under higher stress conditions.

5. Conclusions

A comprehensive microstructure-specific creep model for Ni-based alloys, in particular additively manufactured (AM) alloys, has been developed, considering crucial factors like γ'-phase precipitation, dislocation climb, grain boundary sliding (GBS), and creep cavitation. The model demonstrated excellent agreement with experimental data and provided a deep understanding of the impact of AM-specific heterogeneities on creep behavior. Furthermore, it provides insights into the effect of AM-specific heterogeneities on creep behavior in Ni-based alloys, shedding light on the accelerated transition from secondary to tertiary creep stages in AM alloys, attributed to grain-boundary cavitation. The major conclusions are as follows:

1. The incorporation of creep mechanisms GBS, dislocation climb, as well as the onset of failure by creep cavitation and the precipitation of γ' during the process into the creep modelling framework enabled a comprehensive understanding of the influence of different microstructural heterogeneities on creep behaviour. Combined

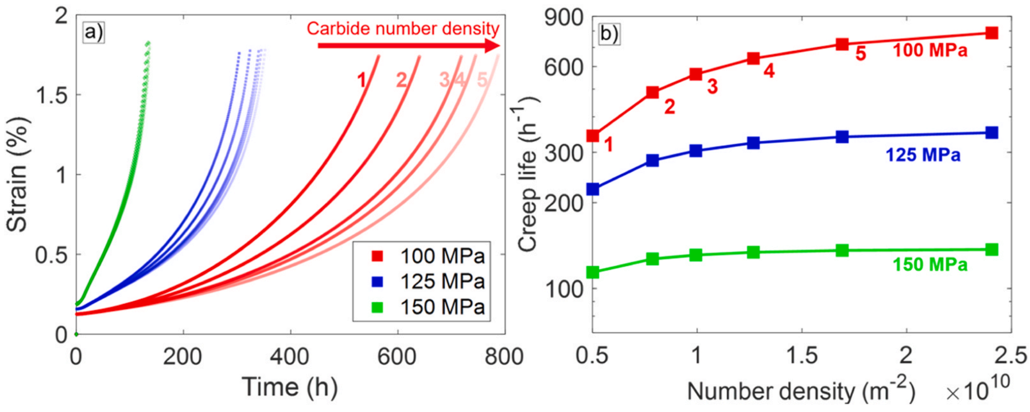

Fig. 11. Effect of the carbide number density at different stresses (100 MPa, 125 MPa and 150 MPa) on the (a) evolution of creep strain over time for different stresses, (b) creep life for AM state at 750 °C based on the numerical model. All parameters were kept constant in the simulation, except for the carbide number density (increased from left to right in (a)) to illustrate the effect of GBS at lower stress (100 MPa).

consideration of in situ γ' precipitation, grain size, and intergranular carbide distribution allowed for quantitative determination of the rate-controlling mechanisms at distinct creep stages.

2. The applied creep model indicates dislocation climb, as opposed to particle shearing or Orowan bowing as the dominant dislocation-particle interaction mechanism in the secondary creep stage.
3. At high stresses (>100 MPa), the accelerated kinetics of creep cavity formation controlled the evolution of tertiary creep, resulting in an early failure of specimens in AM state compared to those in CM state. The smaller grain size and incomplete recrystallization, due to the pinning of grain boundaries by AM-specific primary nanosized intragranular $M_{23}C_6$ carbides, increased the potential nucleation sites for cavities, leading to accelerated tertiary creep in the AM state.
4. At low stress levels (100 MPa), the influence of cavity kinetics was less pronounced, and GBS emerged as the dominant mechanism. The discrete grain-boundary decoration with coarse as well as lower volume fraction of $M_{23}C_6$ carbides in CM state compared to uniform and fine carbides in the AM state led to higher strain rates in the tertiary creep stage, ultimately causing early failure.

CRediT authorship contribution statement

Christian Haase: Writing – review & editing, Supervision, Methodology. **Fuyao Yan:** Writing – review & editing, Supervision, Investigation, Formal analysis. **Ivo Šulák:** Writing – review & editing, Investigation. **Venkatesh Pandian Narayana Samy:** Writing – review & editing, Writing – original draft, Visualization, Software, Methodology, Investigation, Formal analysis, Data curation, Conceptualization. **Frederike Brasche:** Writing – review & editing, Supervision, Conceptualization. **Ida Berglund:** Writing – review & editing, Resources. **Ulrich Krupp:** Writing – review & editing, Supervision, Funding acquisition. **Betül Bezci:** Investigation, Formal analysis. **Benedikt Nowak:** Writing – review & editing, Resources, Investigation.

Declaration of Competing Interest

The authors declare that they have no known competing financial interests or personal relationships that could have appeared to influence the work reported in this paper.

Data availability

Data will be made available on request.

Acknowledgements

The authors also acknowledge Felix Meixner from TU Graz, Austria, for his valuable discussions and expertise in cavity nucleation analysis. The authors would like to acknowledge DESY (Hamburg, Germany), a member of the Helmholtz Association HGF, for the provision of experimental facilities. Synchrotron XRD experiments in the research were carried out at Petra III and we would like to thank Dr. Zoltan Hegedüs at DESY, Dr. Efthymios Polatidis at Paul Scherrer Institut and Ahmet Turnali at RWTH Aachen University. Beamtime was allocated for proposal I-20220679 EC. This research is supported by the funding from the European Union's Horizon 2020 research and innovation program under grant agreement No 958192. CH also acknowledges the support of the German Federal Ministry of Education and Research within the NanoMatFutur project "MatAM - Design of additively manufactured high-performance alloys for automotive applications" (project ID 03XP0264).

Approval of the submitted version of the manuscript

Please check this box to confirm that all co-authors have read and approved the version of the manuscript that is submitted. Signatures are not required.

References

[1] R.C. Reed, The Superalloys: Fundamentals and Applications, Cambridge University Press, Cambridge, 2006, https://doi.org/10.1017/CBO9780511541285.

[2] B. Geddes, H. Leon, X. Huang, Superalloys: Alloying and Performance, ASM International, 2010, https://doi.org/10.31399/asm.tb.sap.9781627083133.

[3] T.M. Smith, C.A. Kantzos, N.A. Zarkevich, B.J. Harder, M. Heczko, P.R. Gradl, A. C. Thompson, M.J. Mills, T.P. Gabb, J.W. Lawson, A 3D printable alloy designed for extreme environments, Nature 617 (2023) 513–518, https://doi.org/10.1038/s41586-023-05893-0.

[4] H. Xue, C. Yang, F. De Geuser, P. Zhang, J. Zhang, B. Chen, F. Liu, Y. Peng, J. Bian, G. Liu, A. Deschamps, J. Sun, Highly stable coherent nanoprecipitates via diffusion-dominated solute uptake and interstitial ordering, Nat. Mater. 22 (2023) 434–441, https://doi.org/10.1038/s41563-022-01420-0.

[5] W.G. Fahrenholtz, G.E. Hilmas, Ultra-high temperature ceramics: materials for extreme environments, Scr. Mater. 129 (2017) 94–99, https://doi.org/10.1016/j.scriptamat.2016.10.018.

[6] C.T. Sims, N.S. Stoloff, W.C. Hagel, Superalloys II, John Wiley & Sons, New York, 1987.

[7] M. Das, P.K. Sen, G. Sahu, R. Sharma, S. Bohidar, Review on high performance nickel based super alloy, Int. J. Eng. Manag. Res. (IJEMR) 5 (2015) 286–291.

[8] M.M. Attallah, R. Jennings, X. Wang, L.N. Carter, Additive manufacturing of Ni-based superalloys: the outstanding issues, MRS Bull. 41 (2016) 758–764, https://doi.org/10.1557/mrs.2016.211.

[9] H. Hamdi, H.R. Abedi, Thermal stability of Ni-based superalloys fabricated through additive manufacturing: a review, J. Mater. Res. Technol. 30 (2024) 4424–4476, https://doi.org/10.1016/j.jmrt.2024.04.161.

[10] T. Hentrich, H. Hattendorf, S. Bellmann, B. Nowak, 2023AMPP-2023-18845., Investig. Microstruct. Stab. Long. -Term. High. -Temp. Expo. Alloy 699 XA.

[11] H. Hattendorf, J. Kloewer, A. López, Alloy 699 XA - A New Alloy for Application Under Metal Dusting Conditions, in: 2018: p. NACE-2018-11200.

[12] T. DebRoy, H.L. Wei, J.S. Zuback, T. Mukherjee, J.W. Elmer, J.O. Milewski, A. M. Beese, A. Wilson-Heid, A. De, W. Zhang, Additive manufacturing of metallic components – process, structure and properties, Prog. Mater. Sci. 92 (2018) 112–224, https://doi.org/10.1016/j.pmatsci.2017.10.001.

[13] A. Mostafaei, R. Ghiaasiaan, I.-T. Ho, S. Strayer, K.-C. Chang, N. Shamsaei, S. Shao, S. Paul, A.-C. Yeh, S. Tin, A.C. To, Additive manufacturing of nickel-based superalloys: a state-of-the-art review on process-structure-defect-property relationship, Prog. Mater. Sci. 136 (2023) 101108, https://doi.org/10.1016/j.pmatsci.2023.101108.

[14] C. Panwisawas, Y.T. Tang, R.C. Reed, Metal 3D printing as a disruptive technology for superalloys, Nat. Commun. 11 (2020) 2327, https://doi.org/10.1038/s41467-020-16188-7.

[15] M. Rahman, W.K.H. Seah, T.T. Teo, The machinability of inconel 718, J. Mater. Process. Technol. 63 (1997) 199–204, https://doi.org/10.1016/S0924-0136(96)02624-6.

[16] M. Attaran, The rise of 3-D printing: the advantages of additive manufacturing over traditional manufacturing, Bus. Horiz. 60 (2017) 677–688, https://doi.org/10.1016/j.bushor.2017.05.011.

[17] M. Gäumann, C. Bezençon, P. Canalis, W. Kurz, Single-crystal laser deposition of superalloys: processing–microstructure maps, Acta Mater. 49 (2001) 1051–1062, https://doi.org/10.1016/S1359-6454(00)00367-0.

[18] S. Li, Q. Wei, Y. Shi, Z. Zhu, D. Zhang, Microstructure characteristics of inconel 625 superalloy manufactured by selective laser melting, J. Mater. Sci. Technol. 31 (2015) 946–952, https://doi.org/10.1016/j.jmst.2014.09.020.

[19] P. Köhnen, M. Létang, M. Voshage, J.H. Schleifenbaum, C. Haase, Understanding the process-microstructure correlations for tailoring the mechanical properties of L-PBF produced austenitic advanced high strength steel, Addit. Manuf. 30 (2019) 100914, https://doi.org/10.1016/j.addma.2019.100914.

[20] X. Zhang, Y. Mu, N. Lu, Q. Li, S. Chen, Y. Zhou, X. Sun, J. Liang, J. Li, Effect of solid solution elements on cracking susceptibility of Ni-based superalloys during additive manufacturing, J. Mater. Sci. Technol. 190 (2024) 218–228, https://doi.org/10.1016/j.jmst.2023.11.073.

[21] N. Kwabena Adomako, N. Haghdadi, S. Primig, Electron and laser-based additive manufacturing of Ni-based superalloys: a review of heterogeneities in microstructure and mechanical properties, Mater. Des. 223 (2022) 111245, https://doi.org/10.1016/j.matdes.2022.111245.

[22] Y. Kok, X.P. Tan, P. Wang, M.L.S. Nai, N.H. Loh, E. Liu, S.B. Tor, Anisotropy and heterogeneity of microstructure and mechanical properties in metal additive manufacturing: a critical review, Mater. Des. 139 (2018) 565–586, https://doi.org/10.1016/j.matdes.2017.11.021.

[23] S. Sen-Britain, S. Cho, S. Kang, Z. Qi, S. Khairallah, D. Rosas, V. Som, T.T. Li, S. Roger Qiu, Y. Morris Wang, B.C. Wood, T. Voisin, Critical role of slags in pitting corrosion of additively manufactured stainless steel in simulated seawater, Nat. Commun. 15 (2024) 867, https://doi.org/10.1038/s41467-024-45120-6.

[24] W. Zhang, A. Chabok, H. Wang, J. Shen, J.P. Oliveira, S. Feng, N. Schell, B.J. Kooi, Y. Pei, Ultra-strong and ductile precipitation-strengthened high entropy alloy with 0.5% Nb addition produced by laser additive manufacturing, J. Mater. Sci. Technol. 187 (2024) 195–211, https://doi.org/10.1016/j.jmst.2023.11.053.

[25] Y.-L. Kuo, S. Horikawa, K. Kakehi, Effects of build direction and heat treatment on creep properties of Ni-base superalloy built up by additive manufacturing, Scr. Mater. 129 (2017) 74–78, https://doi.org/10.1016/j.scriptamat.2016.10.035.

[26] Y.-L. Kuo, S. Horikawa, K. Kakehi, The effect of interdendritic δ phase on the mechanical properties of Alloy 718 built up by additive manufacturing, Mater. Des. 116 (2017) 411–418, https://doi.org/10.1016/j.matdes.2016.12.026.

[27] S.J. Davies, S.P. Jeffs, M.P. Coleman, R.J. Lancaster, Effects of heat treatment on microstructure and creep properties of a laser powder bed fused nickel superalloy, Mater. Des. 159 (2018) 39–46, https://doi.org/10.1016/j.matdes.2018.08.039.

[28] K. Kunze, T. Etter, J. Grässlin, V. Shklover, Texture, anisotropy in microstructure and mechanical properties of IN738LC alloy processed by selective laser melting (SLM), Mater. Sci. Eng.: A 620 (2015) 213–222, https://doi.org/10.1016/j.msea.2014.10.003.

[29] S. Wu, H.Y. Song, H.Z. Peng, P.D. Hodgson, H. Wang, X.H. Wu, Y.M. Zhu, M. C. Lam, A.J. Huang, A microstructure-based creep model for additively manufactured nickel-based superalloys, Acta Mater. 224 (2022) 117528, https://doi.org/10.1016/j.actamat.2021.117528.

[30] E. Hosseini, V.A. Popovich, A review of mechanical properties of additively manufactured Inconel 718, Addit. Manuf. 30 (2019) 100877, https://doi.org/10.1016/j.addma.2019.100877.

[31] M. Pröbstle, S. Neumeier, J. Hopfenmüller, L.P. Freund, T. Niendorf, D. Schwarze, M. Göken, Superior creep strength of a nickel-based superalloy produced by selective laser melting, Mater. Sci. Eng.: A 674 (2016) 299–307, https://doi.org/10.1016/j.msea.2016.07.061.

[32] V.P. Narayana Samy, F. Brasche, I. Šulák, B. Verma, B. Nowak, Z. Chlup, T. Záležák, J.H. Schleifenbaum, U. Krupp, C. Haase, The influence ofmicrostructural heterogeneities on high-temperature mechanical properties ofadditively manufactured γ'-forming Ni-based alloys, Additive Manufacturing 88 (2024) 104267, https://doi.org/10.1016/j.addma.2024.104267.

[33] X. Li, S.R. Holdsworth, S. Kalácska, L. Balogh, J.-S. Park, Y.A.R. Dasilva, X. Maeder, A. Cocks, E. Mazza, E. Hosseini, In-situ and ex-situ microstructure studies and dislocation-based modelling for primary creep regeneration response of 316H stainless steel, Acta Mater. 216 (2021) 117130, https://doi.org/10.1016/j.actamat.2021.117130.

[34] Y.-K. Kim, D. Kim, H.-K. Kim, C.-S. Oh, B.-J. Lee, An intermediate temperature creep model for Ni-based superalloys, Int. J. Plast. 79 (2016) 153–175, https://doi.org/10.1016/j.ijplas.2015.12.008.

[35] A. Drexler, A. Fischersworring-Bunk, B. Oberwinkler, W. Ecker, H.-P. Gänser, A microstructural based creep model applied to alloy 718, Int. J. Plast. 105 (2018) 62–73, https://doi.org/10.1016/j.ijplas.2017.11.003.

[36] W. Xiong, G.B. Olson, Cybermaterials: materials by design and accelerated insertion of materials, NPJ Comput. Mater. 2 (1) (2016) 14, https://doi.org/10.1038/npjcompumats.2015.9.

[37] R.W. Evans, B. Wilshire, Creep behaviour of superalloy blade materials, Mater. Sci. Technol. (U. Kingd.) 3 (1987) 701–705, https://doi.org/10.1179/mst.1987.3.9.701.

[38] L. Méric, P. Poubanne, G. Cailletaud, Single crystal modeling for structural calculations: part 1-model presentation, J. Eng. Mater. Technol., Trans. ASME 113 (1991) 162–170, https://doi.org/10.1115/1.2903374.

[39] J.C. Ion, A. Barbosa, M.F. Ashby, B.F. Dyson, M. McLean, The Modelling of Creep for Engineering Design, Technical Report. National Physical Laboratory, Teddington, UK. (1986).

[40] L. Cui, J. Yu, J. Liu, T. Jin, X. Sun, The creep deformation mechanisms of a newly designed nickel-base superalloy, Mater. Sci. Eng.: A 710 (2018) 309–317, https://doi.org/10.1016/j.msea.2017.11.002.

[41] T.M. Smith, B.S. Good, T.P. Gabb, B.D. Esser, A.J. Egan, L.J. Evans, D.W. McComb, M.J. Mills, Effect of stacking fault segregation and local phase transformations on creep strength in Ni-base superalloys, Acta Mater. 172 (2019) 55–65, https://doi.org/10.1016/j.actamat.2019.04.038.

[42] C. Tian, G. Han, C. Cui, X. Sun, Effects of stacking fault energy on the creep behaviors of Ni-base superalloy, Mater. Des. 64 (2014) 316–323, https://doi.org/10.1016/j.matdes.2014.08.007.

[43] R.R. Unocic, N. Zhou, L. Kovarik, C. Shen, Y. Wang, M.J. Mills, Dislocation decorrelation and relationship to deformation microtwins during creep of a γ' precipitate strengthened Ni-based superalloy, Acta Mater. 59 (2011) 7325–7339, https://doi.org/10.1016/j.actamat.2011.07.069.

[44] J. Coakley, D. Dye, H. Basoalto, Creep and creep modelling of a multimodal nickel-base superalloy, Acta Mater. 59 (2011) 854–863, https://doi.org/10.1016/j.actamat.2010.08.035.

[45] D. Barba, E. Alabort, S. Pedrazzini, D.M. Collins, A.J. Wilkinson, P.A.J. Bagot, M. P. Moody, C. Atkinson, A. Jérusalem, R.C. Reed, On the microtwinning mechanism in a single crystal superalloy, Acta Mater. 135 (2017) 314–329, https://doi.org/10.1016/j.actamat.2017.05.072.

[46] D. Spader, M. Lapera, H. Ghonem, A coupled, physics-based matrix-grain boundary model for creep of carbide strengthened nickel-based superalloys - II. Experimental results and model application, Mater. Sci. Eng.: A 769 (2020) 138355, https://doi.org/10.1016/j.msea.2019.138355.

[47] S.D. Yadav, B. Sonderegger, M. Stracey, C. Poletti, Modelling the creep behaviour of tempered martensitic steel based on a hybrid approach, Mater. Sci. Eng.: A 662 (2016) 330–341, https://doi.org/10.1016/j.msea.2016.03.071.

[48] Q. Jia, Y. Zhuo, Y. Yan, C. Lu, Z. Chen, Y. Cheng, C. Wang, Tensile creep mechanisms of Al-Mn-Sc alloy fabricated by additive manufacturing, Addit. Manuf. 79 (2024) 103910, https://doi.org/10.1016/j.addma.2023.103910.

[49] J.U. Rakhmonov, R. Michi, S. Bahl, O. Rahman, C. Frederick, A.K. Ziabari, D. C. Dunand, R. Dehoff, A. Plotkowski, A. Shyam, Creep deformation and cavitation in an additively manufactured Al-8.6Cu-0.4Mn-0.9Zr (wt%) alloy, Addit. Manuf. 84 (2024) 104097, https://doi.org/10.1016/j.addma.2024.104097.

[50] H. Lukas, S.G. Fries, B. Sundman, Computational Thermodynamics: The Calphad Method, Cambridge University Press, Cambridge, 2007, https://doi.org/10.1017/CBO9780511804137.

[51] Thermo-Calc Software, The Precipitation Module (TC-PRISMA) User Guide 2022a., (2023).

[52] Thermo-Calc Software TCNI12: Ni-Alloys version 12.1, ⟨https://thermocalc.com/products/databases/nickel-based-alloys/⟩ (accessed 06-11-2023), (n.d.).

[53] G.H. Gulliver, The quantitative effect of rapid cooling upon the constitution of binary alloys, J. Inst. Met. 9 (1913).

[54] E. Scheil, Bemerkungen zur Schichtkristallbildung, Int. J. Mater. Res. 34 (1942) 70–72, https://doi.org/10.1515/ijmr-1942-340303.

[55] Thermo-Calc Software MOBNI6: Ni-Alloys Mobility version 6.0, ⟨https://thermocalc.com/products/databases/nickel-based-alloys/⟩ (accessed 06-11-2023).

[56] K.L. Murty, S. Gollapudi, K. Ramaswamy, M.D. Mathew, I. CharitCreep deformation of materials in light water reactors (LWRs) Elsevier , Materials Ageing and Degradation in Light Water Reactors , 2013, , 81–148, 10.1533/9780857097453.1.81.

[57] B.F. Dyson, Microstructure based creep constitutive model for precipitation strengthened alloys: theory and application, Mater. Sci. Technol. 25 (2009) 213–220, https://doi.org/10.1179/174328408X369348.

[58] X.J. Wu, A.K. Koul, Grain boundary sliding in the presence of grain boundary precipitates during transient creep, Met. Mater. Trans. A 26 (1995) 905–914, https://doi.org/10.1007/BF02649087.

[59] M.E. Kassner, Chapter 10 - Creep Fracture, in: M.E. Kassner (Ed.), Fundamentals of Creep in Metals and Alloys (Third Edition), Butterworth-Heinemann, Boston, 2015: pp. 233–260. ⟨https://doi.org/10.1016/B978-0-08-099427-7.00010-4⟩.

[60] Zeldovich, Y.B.; Sunyaev, R. 10. On the Theory of New Phase Formation. Cavitation. In Selected Works of Yakov BorisovichZeldovich, Volume I; Princeton University Press: Princeton, NJ, USA, 1992; pp. 120–137, 2014.

[61] J. Frenkel, A general theory of heterophase fluctuations and pretransition phenomena, J. Chem. Phys. 7 (1939) 538–547, https://doi.org/10.1063/1.1750484.

[62] R. Becker, W. Döring, Kinetische Behandlung der Keimbildung in übersättigten Dämpfen, Ann. Der Phys. 416 (1935) 719–752, https://doi.org/10.1002/andp.19354160806.

[63] M. Volmer, A Weber, Keimbildung in übersättigten Gebilden, Z. F. üR. Phys. Chem. 119U (1926) 277–301, https://doi.org/10.1515/zpch-1926-11927.

[64] F. Meixner, M.R. Ahmadi, C. Sommitsch, Cavity nucleation and growth in nickel-based alloys during creep, Materials 15 (2022) 1495, https://doi.org/10.3390/ma15041495.

[65] F. Meixner, M.R. Ahmadi, C. Sommitsch, Modeling and simulation of pore formation in a bainitic steel during creep, Met. Mater. Trans. A 53 (2022) 984–999, https://doi.org/10.1007/s11661-021-06569-y.

[66] M.R. Ahmadi, B. Sonderegger, S.D. Yadav, M.C. Poletti, Modelling and simulation of diffusion driven pore formation in martensitic steels during creep, Mater. Sci. Eng.: A 712 (2018) 466–477, https://doi.org/10.1016/j.msea.2017.12.010.

[67] B. Dyson, Use of CDM in materials modeling and component creep life prediction, J. Press. Vessel Technol., Trans. ASME 122 (2000) 281–296, https://doi.org/10.1115/1.556185.

[68] H. Basoalto, S.K. Sondhi, B.F. Dyson, M. McLeanA generic microstructure-explicit model of creep in nickel-base superalloys 1 Superalloys. TMS.2004, , 897–906, 10.7449/2004/Superalloys_2004_897_906.

[69] A. Ulbricht, L.A. Ávila Calderón, K. Sommer, G. Mohr, A. Evans, B. Skrotzki, G. Bruno, Evolution of creep damage of 316L produced by laser powder bed fusion, Adv. Eng. Mater. 25 (2023) 2201581, https://doi.org/10.1002/adem.202201581.

[70] Y. Dou, H. Luo, Y. Jiang, X. Tang, Effects of alloying elements on the stacking fault energies of Ni58Cr32Fe10 alloys: a first-principle study, Metals 9 (2019) 1163, https://doi.org/10.3390/met9111163.

[71] N.K. Park, J.J. Kim, Y.S. Chai, H.S. Lee, Microstructural evolution of inconel 690 alloy for steam generator tubes, Key Eng. Mater. 353–358 (2007) 1609–1613, https://doi.org/10.4028/www.scientific.net/KEM.353-358.1609.

[72] R. Resnick, L. Seigle, Nucleation of voids in metals during diffusion and creep, JOM 9 (1957) 87–94, https://doi.org/10.1007/BF03398461.

[73] L. Huang, M. Sauzay, Y. Cui, P. Bonnaille, Theoretical and experimental study of creep damage in alloy 800 at high temperature, Mater. Sci. Eng.: A 813 (2021) 140953, https://doi.org/10.1016/j.msea.2021.140953.

[74] H. Jou, P. Voorhees, G. Olson, Computer Simulations for the Prediction of Microstructure/Property Variation in Aeroturbine Disks, Proceedings of the International Symposium on Superalloys (2004). ⟨https://doi.org/10.7449/2004/Superalloys_2004_877_886⟩.

[75] J. Haan, A. Bezold, C. Broeckmann, Interaction between particle precipitation and creep behavior in the Ni-base Alloy 617B: microstructural observations and constitutive material model, Mater. Sci. Eng.: A 640 (2015) 305–313, https://doi.org/10.1016/j.msea.2015.06.002.

[76] B.F. Dyson, T.B. Gibbons, Tertiary creep in nickel-base superalloys: analysis of experimental data and theoretical synthesis, Acta Metall. 35 (1987) 2355–2369, https://doi.org/10.1016/0001-6160(87)90083-6.

[77] M.H. Yoo, H. Trinkaus, Crack and cavity nucleation at interfaces during creep, Metall, Mater. Trans. A 14 (1983) 547–561, https://doi.org/10.1007/BF02643772.

[78] E.M. Lehockey, G. Palumbo, On the creep behaviour of grain boundary engineered nickel 1, Mater. Sci. Eng.: A 237 (1997) 168–172, https://doi.org/10.1016/S0921-5093(97)00126-3.

[79] J.-S. Zhang13 - Nucleation of Creep Cavity Woodhead Publishing , High Temperature Deformation and Fracture of Materials (ed.) , 2010, , 191–198, 10.1533/9780857090805.2.191, (ed.).

[80] C. Öberg, B. Zhu, S. Jonsson, Creep behaviour, creep damage and precipitation in the austenitic cast steel HK30 at 750 °C, Mater. Sci. Eng.: A 797 (2020) 140253, https://doi.org/10.1016/j.msea.2020.140253.

[81] W. Chen, M.C. Chaturvedi, The effect of grain boundary precipitates on the creep behavior of Inconel 718, Mater. Sci. Eng.: A 183 (1994) 81–89, https://doi.org/10.1016/0921-5093(94)90892-3.

[82] D.A. Woodford, J.J. Frawley, The effect of grain boundary orientation on creep and rupture of IN-738 and nichrome, Metall. Trans. 5 (1974) 2005–2013, https://doi.org/10.1007/BF02644493.

[83] S.L. Mannan, P. Rodriguez, Effect of grain size on creep rate in type 316 stainless steel at 873 and 973 K, Met. Sci. 17 (1983) 63–69, https://doi.org/10.1179/030634583790427595.

[84] Z. Yao, M. Zhang, J. Dong, Stress rupture fracture model and microstructure evolution for waspaloy, Met. Mater. Trans. A 44 (2013) 3084–3098, https://doi.org/10.1007/s11661-013-1660-8.

[85] J.F. Mancuso, C.-Y. Li, The growth of grain boundary cavities under applied stress and internal pressure, Met. Trans. A 10 (1979) 1719–1722, https://doi.org/10.1007/BF02811706.

[86] J. Xu, H. Gruber, D. Deng, R.L. Peng, J.J. Moverare, Short-term creep behavior of an additive manufactured non-weldable Nickel-base superalloy evaluated by slow strain rate testing, Acta Mater. 179 (2019) 142–157, https://doi.org/10.1016/j.actamat.2019.08.034.

[87] L. Thébaud, P. Villechaise, C. Crozet, A. Devaux, D. Béchet, J.-M. Franchet, A.-L. Rouffié, M. Mills, J. Cormier, Is there an optimal grain size for creep resistance in Ni-based disk superalloys, Mater. Sci. Eng.: A 716 (2018) 274–283, https://doi.org/10.1016/j.msea.2017.12.104.